Mathematical Biosciences and Engineering

MBE, 20(7): 12056–12075.
DOI: 10.3934/mbe.2023536
Received: 07 March 2023
Revised: 21 April 2023
Accepted: 26 April 2023
Published: 15 May 2023

http://www.aimspress.com/journal/MBE

*Research article*

# Electrical-thermal coupling characteristics of pre-insertion resistors in AC filter circuit breaker for UHV grid

**Yanyan Bao[1,2], Kang Liu[2], Dingjun Wen[3], Yifan Li[1], Hao Wang[1] and Hongliang Zhang[1,*]**

[1] College of Electrical Engineering and Information Engineering, Lanzhou University of Technology, Lanzhou, China
[2] Electric Power Research Institute of State Grid Gansu Electric Power Company, Lanzhou, China
[3] Party School (Training Center) of State Grid Gansu Electric Power Company, Lanzhou, China

* **Correspondence:** Email: zhanghl312@lut.edu.cn; Tel: +8609312973506; Fax: +8609312973506.

**Abstract:** The ultra-high voltage (UHV) AC/DC grid can provide a platform for sustainable power worldwide. To improve the bus voltage quality of the UHV AC system, AC filters are frequently switched into the UHV grid through circuit breakers with pre-insertion resistors. The pre-insertion resistors suppress inrush currents and operate over-voltage during switching. In this paper, we establish a macro and micro model of the pre-insertion resistor based on its temperature coefficient and micro-morphology. We simulate and analyze its electric-thermal coupling characteristics under standard closing and short-circuit faults. After the simulation model and physical comparison analysis, we find that under a usual closing surge, the electric field distribution of the pre-insertion resistor is uniform and undergoes a slight rise in temperature. However, under a short circuit fault, the temperature rise is drastic and exceeds the maximum allowable temperature, causing glassy melt in some parts of the resistor. Considering the volume ratio of each component of the resistor, a two-dimensional cross-sectional simulation model of the resistor is established to simulate the electric-thermal characteristics of the microstructure of the resistor, and insinuates that the current is concentrated in the carbon channel. That is mainly due to the uneven distribution of carbon material and may lead the local temperature to exceed the maximum allowable temperature and damage the resistor.

**Keywords:** AC filter circuit breaker; pre-insertion resistor; electrical-thermal coupling; ultra-high voltage; smart grid

## 1. Introduction

As clean and sustainable energy, large-scale wind and solar engergy areas are often far from load centers and are integrated through long-distance UHV power grids [1,2]. To mitigate the variability of renewable energy resources, global energy interconnection is proposed to construct an international and intercontinental grid, which is a solid smart grid in a broader range. An ultra-high-voltage direct current (UHV DC) technique is expected to play an important role in the creation of the backbone for Global Energy Internet and in the performance of many functions for the long-range, high-capacity, and high-voltage transmission of renewable energy [3,4]. To reduce the adverse effect of harmonic currents on UHV AC systems and to ensure effective power information within high voltage direct current (HVDC) transmission lines, AC filters must be installed on AC buses [5], and the control strategy for AC filters switching must be optimized according to the actual situation [6,7]. Due to the large capacity and frequent switching of filter banks, circuit breakers for AC filters in DC converter stations must withstand the higher interrupter recovery voltage and break a higher capacitive current. Equipping with a phase selection closing device or a pre-insertion resistor can effectively reduce the closing inrush current and overvoltage, which is helpful to reduce the negative impact on the system, frequent action of the arrester, DC commutation failure, and other adverse consequences [8,9].

At the same time, the digital grid is a new concept of smart grid construction and development driven by technology evolution and demand upgrading, and is the only way for smart grid design and development. At the form level of the digital power grid, it is necessary to use massive intelligent sensors, digital twins, and other technologies to achieve the digital upgrading of the physical power grid. Among them, the digitalization of power equipment is an important aspect and is the basis of its networking and intellectualization. However, under current technical conditions, it is necessary to further promote the integrity of condition assessment data of the power equipment. Therefore, for digital power equipment, sensing technology is not the key, and comprehensive, accurate, and real-time state evaluation of the internal state of power equipment is key. In this paper, the pre-insertion resistor of the circuit breaker is taken as the research object. Through experiments and multi-physical field coupling analysis, the electrical thermal coupling characteristics of the circuit breaker under different working conditions are studied to provide essential support for the digitization of the ultra-high-voltage circuit breaker.

The pre-insertion resistor can absorb part of the electric energy in the grid and convert it into heat energy to weaken the electromagnetic oscillation and limit the overvoltage. Since these breakers must operate automatically and frequently according to load changes, their performance decreases quickly and pre-insertion resistor failures often occur [10,11]. This will seriously affect the smart grid, reduce the quality of the power supply, and cause short circuits and power failures. Additionally, when the long line without load is switched to the UHV grid, a large overvoltage is generated due to a sudden change in the smart grid parameters. To limit this closing overvoltage, pre-insertion resistors are also adopted in UHV line circuit breakers [12]. Although many studies on the pre-insertion resistors of circuit breakers have been carried out from different aspects, the electrical-thermal coupling characteristics of pre-insertion resistors used in AC filter circuit breakers are still unclear. Therefore, to ensure the safe and stable operation of the smart grid for sustainable power, it is of great significance to study the electrical-thermal coupling characteristics of the pre-insertion resistor.

The main contributions of this paper are twofold:

1) The temperature coefficient and microstructure of the resistor are obtained, which provide the

basic parameters for the multi-physical field coupling analysis of the resistor.

2) The reasons for the destruction of the closing resistance under the action of electrothermal coupling are analyzed. When the pre-insertion resistor only passes through the usual closing inrush current, the temperature rise of the closing resistance is not enough to cause thermal shock damage. However, when the pre-insertion resistor passes through the short circuit current, the temperature rise will exceed its maximum allowable temperature. Specifically, the non-uniform distribution of conductive carbon channels in the microscale will further aggravate this temperature rise.

In this paper, an in-depth study of the electrical-thermal coupling characteristics of a pre-insertion resistors of AC filter circuit breakers is carried out. In Section 2, in light of the structure of the AC filter circuit breaker, the relevant characteristics of the pre-insertion resistor are measured and the microstructure of the pre-insertion resistor with and without discharge is observed. In Section 3, a 3D single-phase AC filter circuit breaker model was established and simulated by using the finite element method. In Section 4, the electric and thermal fields of the pre-insertion resistor are analyzed from both the macro and micro aspects.

## 2. Materials and methods

### *2.1. Parameters of pre-insertion resistor*

The pre-insertion resistor is a kind of ceramic carbon, high voltage, high energy, non-inductive resistor, which is made of conductive carbon, bonded clay, and calcined aggregate by high-temperature sintering. The resistor resistivity is usually 70–1000 Ω·cm. There are two purposes for the circuit breaker with the pre-insertion resistor: on the one hand, it can reduce the transient recovery voltage of the main breaker; on the other hand, it can reduce the overvoltage generated by the system when the circuit breaker is closed. The closing resistance of the circuit breaker is generally 400–1500 Ω, and the insertion time is usually around 10 ms. Due to the different relationships between the pre-insertion resistor and the main break, the circuit breaker with a pre-insertion resistor mainly includes a series structure and a parallel structure. The corresponding pre-insertion resistor configuration is shown in Figure 1. This study mainly analyzed the parallel structure.

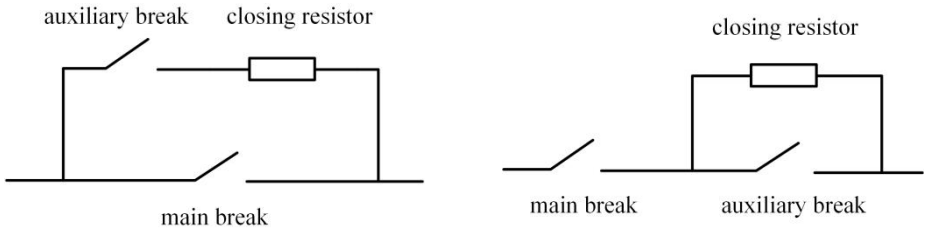


(a) Parallel structure (b) Series structure

**Figure 1.** Pre-insertion resistor configuration diagram.

The auxiliary contact is comprised of three parts: moving contact, static contact, and porcelain

bushing. The pre-insertion resistor and additional contact are connected in parallel with the corresponding arc extinguishing chamber in the circuit. The additional contact needs to operate within a few milliseconds before the closing of the primary contact (arc extinguishing chamber) and then automatically switches off after passing through the tough closing time. K. Chen analyzed the working mechanism of the pre-insertion resistor and gave the method of a pre-test on-site for 1000 kV gas insulated switchgear (GIS) [13]. H. Heiermeier and R. B. Raysaha provided alternative test methods for power testing of pre-insertion resistors without compromising their essential parameters [14]. R. Sun developed a synchronous breaker switching with a pre-insertion resistor to mitigate cap bank switching transients [15]. In recent years, the pre-insertion resistor technique is gradually being replaced by controlled switching devices to suppress switching transients. K. A. Bhatt proposed a new methodology using a controlled switching device with a pre-insertion resistor to further mitigate the switching surge during energization/reenergization of uncompensated transmission lines and shunt reactor compensated transmission lines [16]. R. Li proposed the combination of the vacuum circuit breaker pre-insertion resistor and controlled switching technology, which maximizes the effect of suppression of the inrush current [17]. K. A. Bhatt presented an evaluation of the application of the controlled switching device for reducing the level of inrush current and transient voltage during the energization of an unloaded power transformer using a circuit breaker with a pre-insertion resistor [18]. Although the technology of controlled switching devices has proven useful in switching transmission lines, unloaded power transformers, shunt capacitors, and line reactors, it does not work well for relevant UHV switching operations without a pre-insertion resistor due to the intensive electrical field and lower insulation margin in UHV AC filter circuit breaker.

The pre-insertion resistor must withstand the impulse voltage and absorb the energy of the oscillating wave. The resistance value and the overall dimension of the pre-insertion resistor are required to be high in accuracy to prevent damage caused by uneven loads on the resistor. At the same time, the resistor's ceramic body is porous ceramic, which meets the requirements of resistance to thermal shock. Some resistors may absorb too much energy to exceed their thermal capacity and subsequently burst due to the deviation of the resistance values of different resistors. The performance of the resistor insulation is easy to deteriorate at high temperatures and high voltages, which may lead to the insulation breakdown or damage the coating on the resistor surface [19]. The UHV AC filter circuit breaker can be operated hundreds of times per year. Mechanical vibration caused by frequent operation of the AC filter circuit breaker can significantly increase the probability of either cracking or edge breakage of the pre-insertion resistor, leading to many uncertain discharges. The electrical conductivity and mechanical strength of the resistor body depends on the amounts and arrangement of each phase present, including the conductive, insulators, and pores [20].

The pre-insertion resistor used in the UHV AC filter circuit breaker studied in this paper is produced by HVR International Limited, a predecessor of what is now the British Morgan company. The high-voltage, non-inductive, carbon ceramic linear resistors produced by the HVR Company are made by thoroughly mixing clay, alumina, and carbon. Carbon ceramic resistors are durable, with good flow performance and constant mechanical strength. At the same time, the anti-leakage coating added around the resistor can improve its dielectric tolerance. The pre-insertion resistor is circular, with an inner diameter of 3.4 cm, an outer diameter of 12.7 cm, and a height of 2.54 cm. The resistance of a single piece of the resistor is around 2.6 Ω. The relevant parameters of the pre-insertion resistors are shown in Table 1.

**Table 1.** Pre-insertion resistor related parameters.

| Density (g/cm$^3$) | Volume (cm$^3$) | Specific heat capacity (J·cm$^{-3}$·°C$^{-1}$) | Thermal conductivity (W·m$^{-1}$·K$^{-1}$) |
|---|---|---|---|
| 2.25 | 298 | 2 | 470 |

*2.2. Measurement of temperature coefficient*

The temperature coefficient can directly affect the electrical-thermal coupling characteristics of the pre-insertion resistor. This study sampled and tested the pre-insertion resistor used on site. The specific steps are as follows. First, the model was fixed on the temperature coefficient test device and the resistance value of the model was measured, designated as $R_1$. At the same time, a thermometer was used to measure the temperature of the sample, designated as $T_1$. Second, the temperature coefficient test device was placed in the oven and the desired temperature was set. After the sample was uniformly heated, its resistance value was measured, denoted $R_2$, and the temperature of the sample at the time of measurement was $T_2$. The temperature coefficient was calculated as Eq (2.1).

$$\alpha_R = \frac{R_2 - R_1}{R_1 (T_2 - T_1)} \times 100\% \tag{2.1}$$

where $\alpha_R$ is the temperature coefficient of the model, %/ºC; $R_1$ is the resistance value when the sample temperature is $T_1$, Ω; $R_2$ is the resistance value when the sample temperature is $T_2$, Ω; $T_1$ is the temperature when the measurement resistance is $R_1$, ºC; and $T_2$ is the temperature of the resistance measured after uniform heating, ºC.

*2.3. Microstructure observation*

The microstructure of the broken section at the edge of the resistor was characterized by scanning electron microscope (VE-9800S).

*2.4. Modeling and simulation*

The model used is a single-phase AC filter circuit breaker model. The internal model is a pre-insertion resistor with six connected columns in series. The shell material is a metal conductor with a radius of 80 cm and a height of 100 cm. The COMSOL software was used for simulation and the physical field was selected as the current field. In addition to the three default conditions, the setting of current and potential was added. The current flows in from the column with the least resistors and out from the column with the most resistors. A voltage of 462 kV is applied to the terminal surface where the current flows out, because this voltage is the voltage between phases to the ground. The AC filter circuit breaker shell must be grounded, so the grounding option should also be set. The model is established as shown in Figure 2.

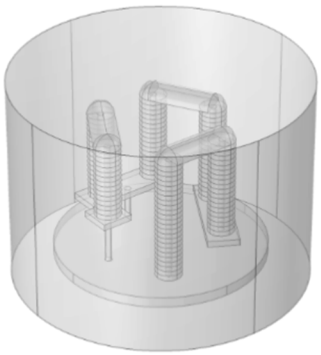

**Figure 2.** GIS model diagram with pre-insertion resistors.

## 3. Results and discussion

### *3.1. Temperature coefficient of resistors*

The method above was used to measure the temperature coefficient of two pre-insertion resistors sampled on-site. The test results are shown in Figure 3. As seen from the figure, when the temperature is lower than 100 ºC, the resistor has a negative temperature coefficient (NTC); when the temperature exceeds 100 ºC, the resistor has a positive temperature coefficient (PTC). On the whole, the temperature coefficient of the resistor is relatively stable with temperature change.

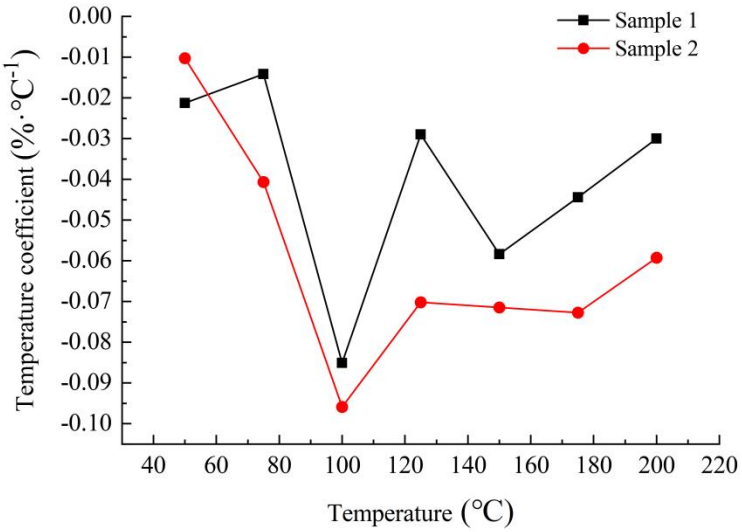


**Figure 3.** Resistivity-temperature characteristic of pre-insertion resistor.

### *3.2. Microstructure of the pre-insertion resistor*

The pre-insertion resistor of the AC filter circuit breaker is pressed on the connecting plate by a spring. According to the design requirements, the spring force is 4964 N. Under normal assembly

conditions, the edge stress of the resistor near the upper part is significantly higher than that of the resistor below. In addition, during the transportation and operation of the resistor, the vibration of the resistor may cause the resistor stack to suffer from an abnormal force, causing the edge of the resistor to be damaged and the discharge of the resistor to be pushed. Figure 4 shows the microstructure of the broken section at the edge of the resistor.

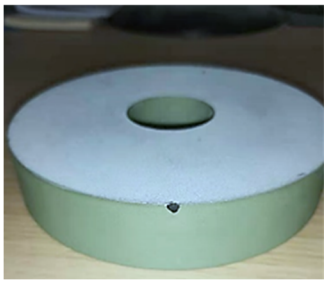

(a) Side notch of the pre-insertion resistor

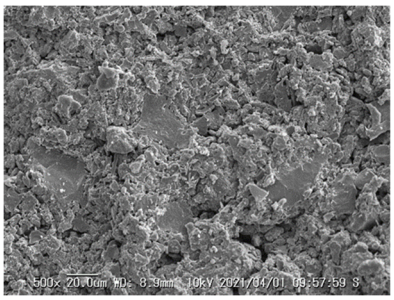

(b) Sectional notch of the pre-insertion resistor

**Figure 4.** Edge chipping and section microstructure of the pre-insertion resistor.

After edge-chipping of the pre-insertion resistor, the electric field distribution around the pre-insertion resistor stack may be distorted, leading to the failure of the surrounding $SF_6$ gas insulation and the short-circuit release of the pre-insertion resistor to the shell. Figure 5 shows the crack of the pre-insertion resistor with breakdown discharge and its microstructure after discharge.

(a) pre-insertion resistor discharge channel

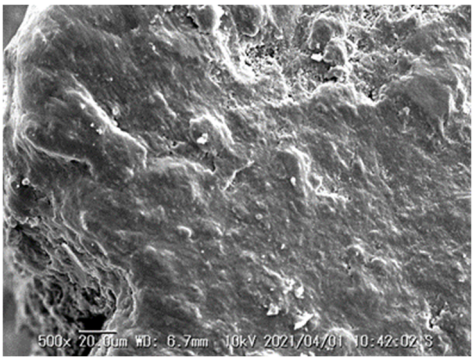

(b) Microstructure diagram of discharge channel of the pre-insertion resistor

**Figure 5.** Discharge damage of the pre-insertion resistor and microstructure of discharge channel.

By comparing Figures 3 and 4, it can be seen that the edge section of the pre-insertion resistor without discharge is a ceramic structure with an aggregate, sintered clay binder, and evenly distributed

pores, and the surface crystallization is complete without an ablation trace. Therefore, it can be inferred that the bottom and sides notches are all mechanical damages caused by external forces. After the discharge channel appears on the pre-insertion resistor, it can be seen from its microscopic morphology that the high-resistance glaze forms a continuous and smooth glassy state at the beginning of the channel, and the discharge leads to the glaze layer to melt into a glass state.

### *3.3. Macro and micro simulation of resistors*

The primary function of the digital power equipment is real-time digital mapping of its state. However, under existing sensor technology, most of the physical quantities inside the power equipment cannot be directly obtained in real time. For example, it is tough to measure the temperature distribution of power equipment, such as transformers and GIS, in real time during either regular operation or fault. Fortunately, the multi-physical field coupling simulation can provide an effective means for the digitalization of power equipment in the development of the smart grid. Li Huang et al. established a digital twin model of transformer windings and analyzed the heat distribution characteristics based on transformer winding losses, which can provide support for internal temperature monitoring and transformer analysis [21]. To replicate the loss density distribution and thermal performance of high-frequency transformers, Wang et al. proposed a digital twin model of power electronic high-frequency transformers (HFT) based on electromagnetic-thermal analysis [22]. Song et al. combined the streamer simulation at the micro level and the circuit simulation model at the macro level to simulate the influence of temperature on the discharge signals of GIS insulation void defects, which can provide a reference for the digital twin model of power equipment status [23].

For the pre-insertion resistor, the electrical-thermal field during operation and fault cannot be directly obtained. Nonetheless, the mapping model of its operation state and electric thermal area can be established through simulation analysis, which provides a reference for the digital twin of a pre-insertion resistor. To simulate the electric field distribution and temperature distribution of the pre-insertion resistor of the circuit breaker in the actual operation process, the electric field strength and temperature of the resistor surface under the opening and closing action are usually studied using the existing multi-physical field simulation software in modern design methods. Through simulation, not only can specific values be obtained, but the relationships between different regions can also be clarified so that the electrical-thermal coupling characteristics of the pre-insertion resistor are more intuitive and easier to analyze, which would significantly improve the accuracy of the conclusion.

The multi-physical area simulation platform provides the function of simulating a single physical field and coupling multiple physical fields, which makes the simulation test run more convenient. To accurately simulate and analyze actual equipment, it is necessary to consider the interaction of multiple physical fields. This study used simulation software to couple the electric field and the heat transfer field to perform simulation analysis that was difficult to achieve using traditional methods.

#### 3.3.1. Electric field simulation

The entire solution domain electric field control equation is given in the following equation:

$$\begin{cases} \nabla \cdot J = Q_{j,v} \\ J = \left(\sigma + \varepsilon_0 \varepsilon_r \dfrac{\partial}{\partial t}\right) E + J_e \\ E = -\nabla V \end{cases} \tag{3.1}$$

where $\sigma$ is the conductivity; $\varepsilon_0$ and $\varepsilon_r$ are the vacuum permittivity and relative permittivity respectively; $J$ is the current density; $J_e$ is the external injection current density; $Q_{j,v}$ is the current or voltage source; $E$ is the electric field strength; and $V$ is the potential. The conductivity of a conductor usually becomes progressively more prominent with increasing temperature. In contrast, the change in conductivity of the material of the pre-insertion resistor sheet in this paper has a minimal effect on the Joule heat loss in the temperature rise range studied, so it is set as a constant.

GIS is a coaxial cylindrical structure. The capacitance of a coaxial cylindrical system can be calculated by using the relationship between the potential difference and the charge. For a coaxial cylindrical system, we can assume that the inner and outer conductors have opposite charges $Q$, the radius of the inner conductor is $r_1$, the radius of the outer conductor is $r_2$, and there is a medium between them with a permittivity of $\varepsilon_r$. The capacitance per unit length of the coaxial cylindrical system is

$$C = \frac{Q}{U} = \frac{2\pi\varepsilon}{\ln \dfrac{r_2}{r_1}} \tag{3.2}$$

where $Q$ is charges of inner and outer conductors, and $U$ is the potential between the two conductors.

For a coaxial cylindrical system, we can choose a cylindrical Gaussian surface with radius $r$ and length $l$ that is concentric with the system. The electric field has the same magnitude and direction at every point on this surface, and is perpendicular to the surface. The net charge enclosed by the Gaussian surface depends on whether $r$ is smaller than, equal to, or larger than the radius of the inner cylinder $r_1$ or the outer cylinder $r_2$. If $r < r_1$, then there is no charge enclosed and the electric field is zero. If $r_1 < r < r_2$, then only the charge on the inner cylinder is enclosed and the electric field is given by

$$E = \frac{\lambda l}{2\pi\varepsilon_r\varepsilon_0 r} \tag{3.3}$$

where $\lambda$ is the linear charge density of the inner cylinder.

According to Eqs (3.2) and (3.3), if $r_1 < r < r_2$, the electric field in a coaxial cylindrical system can be calculated as follows:

$$E(r) = \frac{U}{r \ln \dfrac{r_2}{r_1}} \tag{3.4}$$

If there is only one column of resistors in GIS with 462 kV applied, the electrical field of the resistors' surface is about 28.71 kV/cm according to Eq (3.4), where $U$ = 462 kV, $r = r_1$ = 6.35 cm, $r_2$ = 80 cm. In GIS, there are six column resistors that shield each other, and the equivalent radius of the resistors will increase to around 3.5 times the diameter of a single resistor. Therefore, the electrical field of the resistors' surface decrease to 17.68 kV/cm. The relationship between the $SF_6$ breakdown field strength and the absolute air pressure under power frequency voltage can be calculated by Eq (3.5):

$$E_{bt} = 6510P^{0.73} \tag{3.5}$$

where $E_{bt}$ is the breakdown field strength (kV/cm) and $P$ is the total gas pressure (MPa). The absolute pressure of $SF_6$ in the UHV AC filter circuit breaker is 0.6 MPa, and the breakdown field strength is 240 kV/cm. According to the coaxial cylindrical insulation structure, the analytical calculation shows that the electric field strength on the surface of the resistor stack inside the GIS is smaller than the breakdown field strength in the $SF_6$ gas. However, the analytical solution does not consider the voltage drop and the shielding effect of the resistor stack base plate after the current flow.

With an applied 462 kV and 420 A closing inrush, the electric field simulation results are shown in Figure 6, where the current inflow end is at the highest potential and the current outflow end is at the lowest potential. When the current does not change, the voltage drop generated on each resistor is consistent. Figure 7 shows a graph of the voltage drop across a single resistor, which does not change over time. The cloud map of the electric field intensity distribution of the entire 3D simulation model is shown in Figure 8. The AC filter circuit breaker with a pre-insertion resistor is filled with $SF_6$ gas to ensure insulation strength. The electrical field strength on the outer surface of the resistor is 0.43 kV/cm, which is less than the breakdown strength under the $SF_6$ power frequency. Therefore, no insulation breakdown will occur inside the circuit breaker with a pre-insertion resistor after the closing operation.

The calculation of the maximum working electric field that the withstands capacity of the resistor of in the $SF_6$ medium is shown in Eq (3.6).

$$V_{wk} = 1.0 \times \frac{RA}{tL}^{0.335} \tag{3.6}$$

where, $V_{wk}$ is the practical value (kV/cm) of the maximum working voltage of the resistor, $R$ is the resistance value (Ω), $A$ is the cross-sectional area ($cm^2$) of the resistor, $t$ is the insertion time (ms), and $L$ is the height (cm) of the resistor. The maximum bearing capacity of the resistor with an insertion time of 10 ms and an outer diameter of 12.7 cm is 2.3 kV/cm. The simulation results show that the overall field strength of the resistor is 0.43 kV/cm, which does not exceed its maximum bearing capacity, so the pre-insertion resistor cannot be broken down.

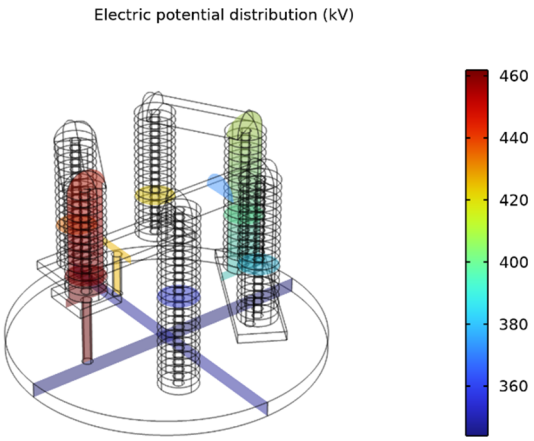


**Figure 6.** The electric potential distribution of the GIS with pre-insertion resistors.

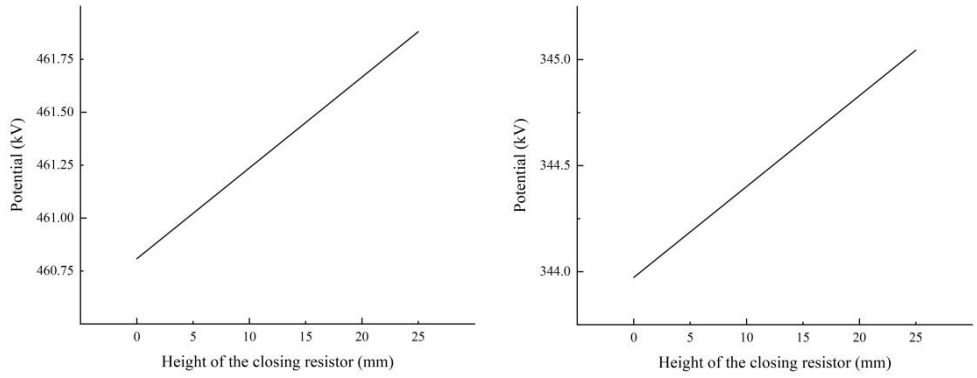


(a) Voltage drop on the head resistor (b) Voltage drop on the end resistor

**Figure 7.** Voltage drop on the resistor at both ends under 420A.

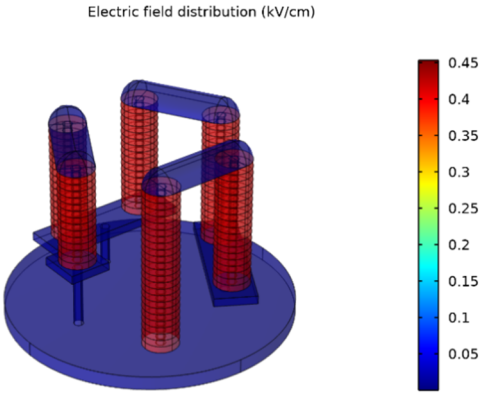


**Figure 8.** The electric field intensity of the GIS with pre-insertion resistors.

### 3.3.2. Electrical -thermal field simulation

During the closing operation of the circuit breaker, the energy injected into the pre-insertion resistor is a function of the applied voltage, resistance value, and current duration. It is difficult to accurately calculate the energy injected because the closing resistance value is slightly different from the nominal value after manufacturing. For convenience, the resistance value is assumed to be equal to its smaller value for a concise period of time during an operation. When the applied current is a sine wave, the energy injected into the unit volume of the resistance can be calculated according to Eq (3.7).

$$W = \frac{U^2}{\omega RV}\left[\omega(t_2 - t_1) - sin\omega(t_2 - t_1)cos\omega(t_2 - t_1)\right] \tag{3.7}$$

where, $U$ is the practical value of the applied voltage; $t_1$ and $t_2$ are the starting and end time of the current, respectively; $\omega$ is the angular frequency of the applied voltage; $\omega$ = 314rad/s under power frequency conditions; $V$ is the resistance volume; and $R$ is the nominal value of the pre-insertion resistor. If $\omega$ ($t_2$ - $t_1$) = $n\pi$, that is, when the current time is $n$ half-waves, there is

$$W = \frac{nU^2}{100RV} \tag{3.8}$$

The resistance is usually considered adiabatic in the process of energy injection due to the short current flow time. The injection energy calculated per unit volume of the pre-insertion resistor with nominal resistance of 2.6 Ω is 7.7 J/cm$^3$.

From the data introduction, the thermodynamic parameters related to pre-insertion resistors are as follows: for resistors ≤ 11.2 cm in diameter, the maximum injection energy ≤ 600 J/cm$^3$ (irregular operation), and the recommended operating temperature ≤ 300 ºC (irregular operation); for resistors > 11.2 cm in diameter, the maximum injection energy ≤ 500 J/cm$^3$ (irregular operation) and the recommended operating temperature ≤ 250 ºC (infrequent operation); and for resistors of all specifications, the recommended operating temperature ≤ 150 ºC (continuous operation).

Under normal operating conditions, the injection energy is below 400 J/cm$^3$, which does not exceed the maximum value. Therefore, the pre-insertion resistor has a large margin in the unit volume energy injection.

According to the heat transfer theory, the controlling equation for the three-dimensional transient heat transfer of the object of study is expressed as：

$$\begin{cases} \rho C_p \dfrac{\partial T}{\partial t} + \rho C_p u \cdot \nabla T + \nabla \cdot q = Q + q_0 + Q_{ted} \\ q = -k\nabla T \end{cases} \tag{3.9}$$

where, $\rho$ is the material density; $C_p$ is the heat capacity of the material; $T$ is the object temperature; $\nabla T$ is the temperature gradient; $u$ is the velocity vector; $q$ is the heat conduction rate; $k$ is the thermal conductivity of the material; $Q_{ted}$ is the increased heat source heat; $q_0$ is the convective heat flux; $q$ is the heat generating power per unit volume and its value is the dot product of $E$ and $J$ in the electric field control equation.

The convective heat flux is expressed as：

$$q_0 = hT_{ext} - T \tag{3.10}$$

where, $h$ is the convective heat transfer coefficient on the outer surface of the circuit breaker, indicating the heat exchange capacity between the outer surface of the circuit breaker and the external atmosphere. Its physical meaning is the convective heat transfer per unit area per unit time when the temperature difference between different objects is 1 K. Its value is mainly related to the relevant flow rate; when there is little or no air flow in the space, the convective heat transfer coefficient is between 5–10 (W/m$^2$·K). $T_{ext}$ is the outside temperature and $T$ is the internal object temperature.

Similar to the boundary condition of the electric field, joule heat will be generated when current flows through the series pre-insertion resistor. The temperature distribution of the pre-insertion resistor at 10 ms is shown in Figure 9. The temperature rise occurs mainly in the pre-insertion resistor because the conductivity of the pre-insertion resistor is less than that of other metal materials, that is, the pre-insertion resistor has a greater resistance to the current, resulting in greater joule heat than metal materials. The temperature distribution demonstrates that the power energy of switching transients can effectively be absorbed by the pre-insertion resistors.

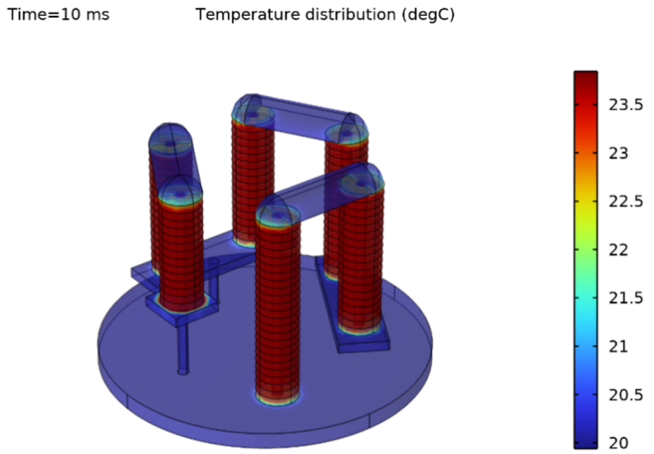


**Figure 9.** Pre-insertion resistor temperature distribution at 10 ms.

The temperature distribution on the surface of the current inflow end and the outflow end is shown in Figure 10. The pre-insertion resistors are stacked in series, and the current flowing through them is the same, so the temperature distribution of the two is similar: the temperature on the outside and inside of the resistor is slightly lower than that in the middle.

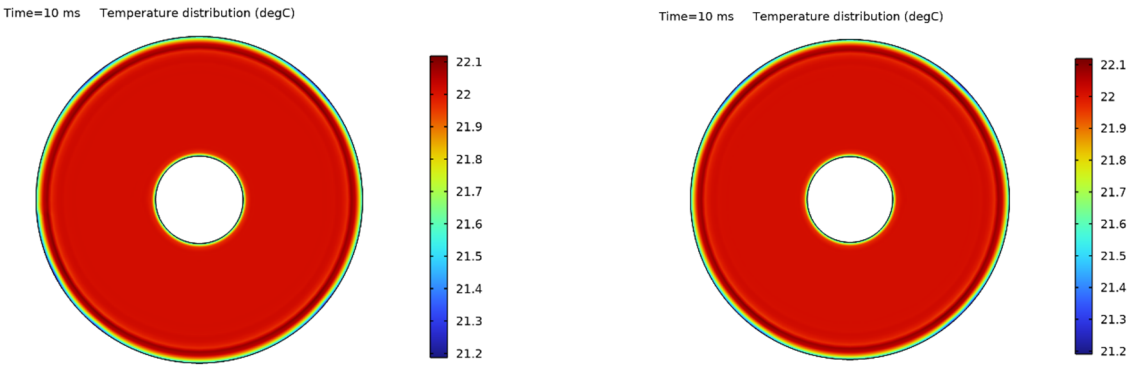


(a) Current inflow end surface

(b) Current outflow end surface

**Figure 10.** Surface temperature distribution cloud map of current terminal.

To further study the temperature variation on the resistors, the outer edge of 24 columns were selected as the research object to observe the temperature change. Temperature variation with time is shown in Figure 11. Results show that at the same time, the temperature in the middle of the outer surface of the resistor stack are constant, the temperature near the bottom and top metal plates will decrease, and the temperature will close; the temperature will reach the maximum value of 5mm near the metal plate side. The cloud diagram of the temperature distribution of the intermediate resistance surface is shown in Figure 12. Since the resistor chip is close to the resistor chip, the surface temperature is stable at a fixed value, which corresponds to the moderate temperature of the curve at 10 ms in Figure 12.

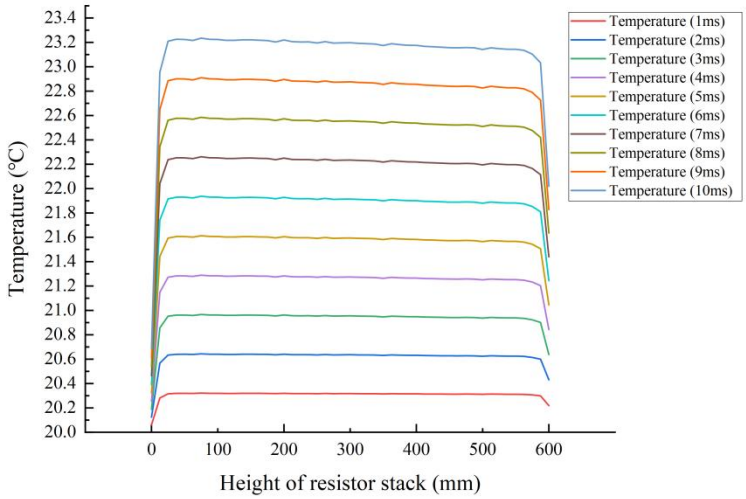


**Figure 11.** Outer bus temperature distribution cloud map.

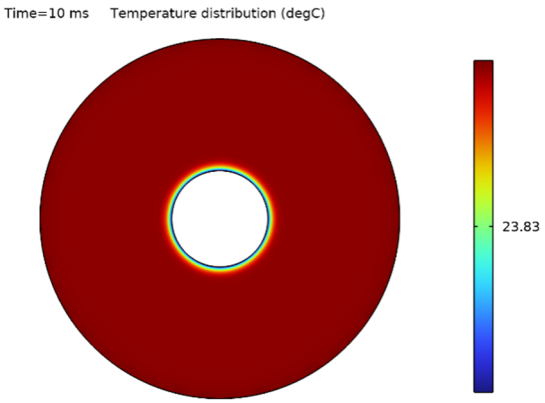


**Figure 12.** Intermediate surface temperature distribution cloud map.

3.3.3. Calculation of the temperature rise of the pre-insertion resistor under fault condition

During the closing operation of the circuit breaker, the energy injected into the pre-insertion resistor is a function of the applied current, resistance value, and the current passing time. According to Joule's law, when the applied current is given, the energy injected into the resistor can be calculated according to Eq (3.11).

$$Q = \int_{t_1}^{t_2} I^2(t) R(t) dt \tag{3.11}$$

when the applied current is a power frequency alternating current, Eq (3.9) can be changed to Eq (3.12).

$$Q = \frac{i}{\sqrt{2}}^2 R\Delta t \tag{3.12}$$

where $Q$ is the energy injected into the resistor; $t_1$ and $t_2$ are the starting and end times of the current

flow, respectively; $I$ is the practical value of the applied current; $i$ is the peak value of the applied current; $R$ is the closing resistance; and $\Delta t$ is the current time.

The calculation equation for the temperature increase caused by the injection of energy is shown in Eq (3.13).

$$\Delta T = \frac{Q}{C_m \cdot V} \tag{3.13}$$

where $\Delta T$ is the temperature increase of the resistor, ℃; $Q$ is the energy absorbed by the single resistor, J; $C_m$ is the specific heat capacity of the resistor, $J \cdot cm^{-3} \cdot ℃^{-1}$; and $V$ is the volume of the single resistor, $cm^3$.

The relationship between the current on the resistor and the temperature at 10 ms under theoretical conditions can be calculated from Eqs (3.12) and (3.13), as shown in Figure 13. The temperature rise of the resistor is 3.85 ºC after 10 ms of current flow, which is in good agreement with the simulation results. Under the application of tens of kA current, the temperature of the pre-insertion resistor can rise to thousands of ℃, which will cause the resistor to melt. This is consistent with the micro morphological change of the resistor with the discharge fault mentioned above.

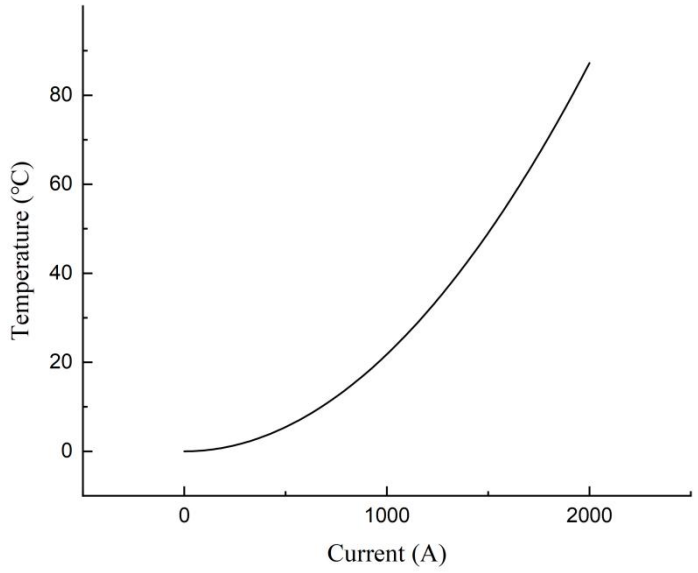


**Figure 13.** Current-Temperature graph.

It can be seen from the above analysis that under normal switching conditions, the closing inrush current of the pre-insertion resistor is small, and the temperature rise of the resistor is not severe, which is far lower than the maximum operating temperature of the resistor. However, when the pre-insertion resistor is in the fault operation state, the $SF_6$ gas around the pre-insertion resistor may discharge, resulting in a short-circuit discharge of the resistor. The maximum short-circuit discharge current can reach tens of kA. Figure 14 shows the temperature distribution of the AC of $4 \times 10^4$A under the fault condition. The temperature rise is as high as $3.47 \times 10^4$ ºC, which is far beyond the allowable temperature rise of the resistor and is sufficient to ablate its surface.

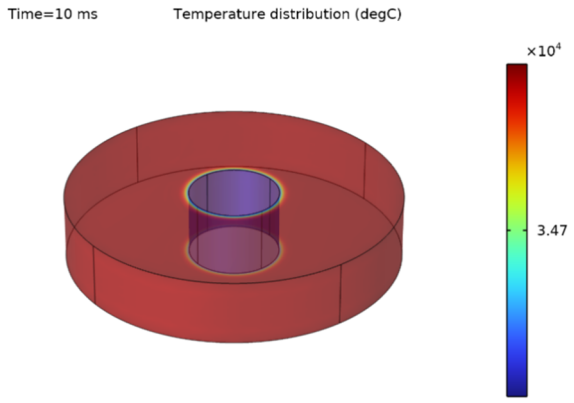


**Figure 14.** Cloud map of temperature distribution under fault current.

### 3.3.4. Micro simulation of resistors

It can be seen from the above results, under the regular closing operation, the temperature change of the resistor has a specific rule. From the sintering characteristics, carbon and ceramics are evenly distributed in the microstructure. After discharge ablation, the temperature increases to make the ceramic glaze layer melt, showing a glassy state. To explore the electrical-thermal characteristics of the internal micro structure of the resistor, a two-dimensional cross-sectional simulation model of the resistor is established, as shown in Figure 15. A single grid represents a material molecule, and the primary materials include carbon molecules, ceramic molecules, and air gaps.

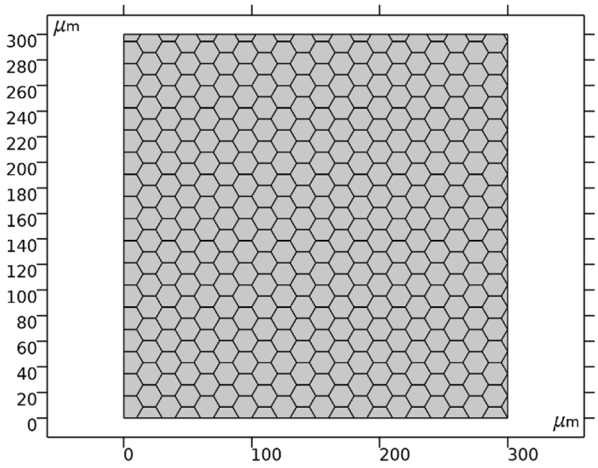


**Figure 15.** Cross-section 2D simulation diagram.

The cross-sectional material setting is similar to that in the microscopic observation figure. The proportion of the three mass fractions is obtained by referring to the relevant literature. According to the corresponding material density, the volume ratio of air gap: ceramic: carbon is 25:42:33. After applying the boundary conditions to the model, the current density distribution of the two-dimensional model is shown in Figure 16. As seen in the figure, the current in the pre-insertion resistor is

concentrated in the carbon channel. The current distribution in the carbon channel is uneven due to the influence of the channel direction. The current density at the interface of carbon particles is most concentrated.

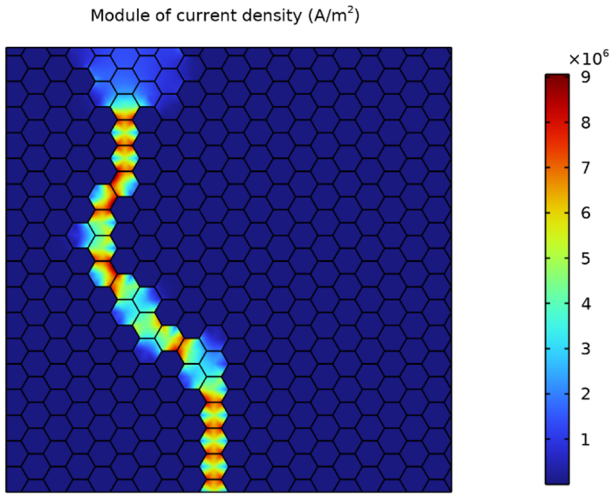


**Figure 16.** Current density distribution cloud map.

The relationship between current density and temperature after applying different currents to the two-dimensional model above is shown in Figure 17.

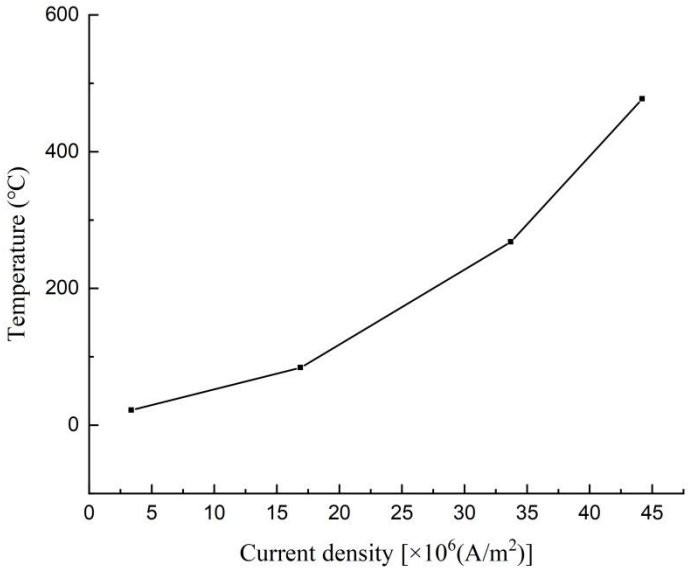


**Figure 17.** Current Density-Temperature graph.

When the short-circuit current is $4 \times 10^4$ A, the average current density on the surface of the resistor is $3.40 \times 10^6$ A/m$^2$. However, carbon only accounts for 33% of the volume of the resistor, and the effective conductive area of the resistor surface will be smaller than the actual area, resulting in the current density in the carbon channel being much larger than $3.40 \times 10^6$ A/m$^2$. As seen in Figure 17,

when the local average current density is greater than $3.37 \times 10^7 A/m^2$, the short-term increase of the average temperature can reach 250 ºC, which exceeds the recommended working temperature of the resistor. Consequently, the resistor is easily damaged under this condition. According to the analysis above, when the carbon distribution inside the resistor is uneven, the local temperature inside the resistor will exceed the maximum allowable temperature of the resistor, causing damage to the resistor.

With the electrical-thermal coupling analysis model of the resistor from the macro and micro aspects, the digital twin model of the UHV pre-insertion resistor can be established by determining the input and output parameters and by using model reduction methods. This will provide a device layer sensing means for the digitalization of power equipment in the smart grid.

## 4. Conclusions

This paper analyzes the electrical-thermal characteristics of the pre-insertion resistor of UHV AC filter circuit breaker using multiphysics field simulation software. The following conclusions are obtained.

Under regular closing operation, the energy injected into the resistor is 2.29 kJ, and the corresponding increase of the temperature in the resistor is 3.85 ºC. Compared to the maximum allowable temperature increase of the pre-insertion resistor of 250 ºC, the thermal capacity of the pre-insertion resistor has an extensive safety margin.

After a short-circuit fault occurs on the pre-insertion resistor, the relationship curve between the local average current density and the average temperature is approximately a quadratic function. Because the current density is concentrated on the carbon channel, the current density at the contact of two adjacent carbon molecules under a single track reaches the maximum, causing the temperature to rise inside the resistor that exceeds the allowable temperature, thus causing the resistor to melt locally. From a micro-point of view, the local overheating inside the resistor often occurs in the place where the carbon molecules gather.

Future work will focus on the experimental validation of the proposed model for the pre-insertion resistor in the field. At the same time, in the future operation of the AC filter circuit breaker, the electric field and temperature of a pre-insertion resistor may be monitored with the development of sensor technology and compared with the digital twin model to form a differentiated evaluation result.

## Acknowledgments

This work was supported by Gansu Provincial Natural Science Foundation of China (21JR7RA237), Gansu Provincial Science and Technology Commissioner Special Project (22CX8GA111) and the SGCC research program.

## Conflict of interest

The authors declare that the research was conducted in the absence of any commercial or financial relationships that could be construed as a potential conflict of interest.

## References


1. B. Alamri, M. A. Hossain, M. S. J. Asghar, Electric power network interconnection: A review on current status, future prospects and research direction, *Electronics*, **10** (2021), 2179. https://doi.org/10.3390/electronics10172179
2. M. Zubair, A. B. Awan, Economic viability of solar energy export from the Middle East and North Africa to Europe and South Asia, *Environ. Dev. Sustainability*, **23** (2021), 17986–18007. https://doi.org/10.1007/s10668-021-01424-x
3. Z. Zhou, Y. Zhang, W. Wang, Research on the development of UHV-DC technology standardization for global energy interconnection, in *2021 IEEE/IAS Industrial and Commercial Power System Asia (I&CPS Asia)*, IEEE, (2021), 1278–1284. https://doi.org/10.1109/ICPSAsia52756.2021.9621534
4. K. Strunz, M. Kuschke, S. Schilling, Climate-friendly and socially inclusive AC-DC renewable energy system with overlay multi-terminal HVDC network (OVANET): Solution with fully distributed optimization and infrastructure combination, *Int. J. Electr. Power Energy Syst.*, **132** (2021), 106119, https://doi.org/10.1016/j.ijepes.2020.106119
5. C. Wang, F. Shi, H. Wang, Q. Yang, Optimization design of AC filters for HVDC systems based on improved particle swarm optimization algorithm, in *IOP Conference Series: Earth and Environmental Science*, IOP Publishing, **453** (2020). https://doi.org/10.1088/1755-1315/453/1/012042.
6. Y. Xue, X. P. Zhang, C. Yang, AC filterless flexible LCC HVDC with reduced voltage rating of controllable capacitors, *IEEE Trans. Power Syst.*, **33** (2018), 5507–5518. https://doi.org/10.1109/tpwrs.2018.2800666
7. H. Li, X. Wang, B. Yu, H. Liu, H. Xu, S. Guo, Improved control strategy for AC-filters switching in UHVDC converter station, in *IOP Conference Series: Earth and Environmental Science*, **192** (2018), 012022. https://doi.org/10.1088/1755-1315/192/1/012022
8. Z. Xiong, L. Zhou, Y. Li, D. Ding, W. Lu, Y. Gao, Study on protection logic of last circuit breaker in ultra high voltage converter station, in *2020 5th Asia Conference on Power and Electrical Engineering (ACPEE)*, (2020), 1651–1656. https://doi.org/10.1109/ACPEE48638.2020.9136325
9. X. Chen, C. He, J. Deng, X. Zhu, G. Zhang, H. Ni, et al., Energization transient suppression of 750 kV AC filters using a pre-insertion resistor circuit breaker with a controlled switching device, *IEEE Trans. Power Delivery*, **37** (2022), 3381–3390. https://doi.org/10.1109/tpwrd.2021.3128617
10. Q. Xin, X. Zhao, D. Xu, L. Guo, Study on the influence of converter transformer magnetizing inrush current on the low-order AC filter, in *2020 5th Asia Conference on Power and Electrical Engineering (ACPEE)*, (2020), 1891–1897. https://doi.org/10.1109/ACPEE48638.2020.9136366
11. M. A. Haseeb, M. J. Thomas, Disconnector switching induced transient voltage and radiated fields in a 1100 kV gas insulated substation, *Electr. Power Syst. Res.*, **161** (2018), 86–94. https://doi.org/10.1016/j.epsr.2018.04.001
12. U. Riechert, W. Holaus, Ultra high-voltage gas-insulated switchgear—a technology milestone, *Eur. Trans. Electr. Power*, **22** (2012), 60–82. https://doi.org/10.1002/etep.582
13. K. Chen, Y. Xu, T. Guo, L. Wang, L. Sun, N. Geng, et al., Working principle and testing technology of circuit breaker pre-insertion resistor for 1100kV GIS, in *IOP Conference Series: Earth and Environmental Science*, **330** (2019), 052006. https://doi.org/10.1088/1755-1315/330/5/052006

14. H. Heiermeier, R. B. Raysaha, Power Testing of pre-insertion resistors: Limitations and Solution, *IEEE Trans. Power Delivery*, **32** (2017), 1688–1695. https://doi.org/10.1109/tpwrd.2016.2519604
15. R. Sun, M. McVey, D. Yang, J. R. Stage, A study of synchronous breaker switching with pre-insertion resistor for capacitors banks, *IEEE Trans. Power Delivery*, **33** (2018), 821–829. https://doi.org/10.1109/tpwrd.2017.2735863
16. K. A. Bhatt, B. R. Bhalja, U. Parikh, Controlled switching technique for minimization of switching surge during energization of uncompensated and shunt compensated transmission lines for circuit breakers having pre-insertion resistors, *Int. J. Electr. Power Energy Syst.*, **103** (2018), 347–359. https://doi.org/10.1016/j.ijepes.2018.06.024
17. R. Li, H. Liu, M. Liao, Y. Jing, X. Duan, K. Li, Investigation on transformer inrush current switched by controlled vacuum circuit breaker, in *2018 28th International Symposium on Discharges and Electrical Insulation in Vacuum (ISDEIV)*, **2** (2018), 563–566. https://doi.org/10.1109/DEIV.2018.8537037
18. K. A. Bhatt, B. R. Bhalja, U. B. Parikh, Evaluation of controlled energisation of an unloaded power transformer for minimising the level of inrush current and transient voltage distortion using PIR-CBs, *IET Gener. Transm. Distrib.*, **12** (2018), 2788–2798. https://doi.org/10.1049/iet-gtd.2017.1825
19. R. Chen, J. Song, L. Hao, Z. Xu, K. Li, W. Chen, et al., Research on mixing process of carbon-ceramic resistor disc for high voltage switchgear, *High Voltage Appar.*, **57** (2021), 196–201.
20. A. M. Bondar, I. Iordache, P. Svasta, Carbon/ceramic composites designed for electronic application, in *2006 1st Electronic Systemintegration Technology Conference*, IEEE, **2** (2006), 708–713. https://doi.org/10.1109/ESTC.2006.280089
21. L. Huang, P. Shen, T. Chen, Y. Li, X. Sun, L. Ju, et al., Digital twin modeling and temperature field analysis of transformer windings, in *2022 IEEE 6th Advanced Information Technology, Electronic and Automation Control Conference (IAEAC)*, (2022), 819–824. https://doi.org/10.1109/iaeac54830.2022.9929698
22. Z. Wang, C. L. Bak, H. Sørensen, F. F. da Silva, Q. Wang, Digital twin modeling and simulation of the high-frequency transformer based on electromagnetic-thermal coupling analysis, in *2022 21st IEEE Intersociety Conference on Thermal and Thermomechanical Phenomena in Electronic Systems (iTherm)*, (2022), 1–7. https://doi.org/10.1109/itherm54085.2022.9899628
23. H. Song, Z. Zhang, J. Tian, G. Sheng, X. Jiang, Multiscale fusion simulation of the influence of temperature on the partial discharge signal of GIS insulation void defects, *IEEE Trans. Power Delivery*, **37** (2022), 1304–1314. https://doi.org/10.1109/TPWRD.2021.3083736


AIMS Press